Stability Analysis of Concrete Gravity Dams under Uncertainty

***Binod K. Yadav*[1] *and Rafi L. Muhanna*[2]**

[1]*Federal Energy Regulatory Commission, Atlanta, GA USA, binod.yadav@ferc.gov*

[2]*Department of Civil and Environmental Engineering, Georgia Institute of Technology, North Avenue, Atlanta, Georgia, 30332, USA, rafi.muhanna@gatech.edu*

Abstract: The stability analysis of concrete gravity dams is challenging due to uncertainties in shear strength parameters and external loads. Conventional crack-based Limit Equilibrium Methods (LEM), which rely on the linear Mohr–Coulomb (MC) shear strength model, often yield conservative results because they neglect nonlinear strength gain from joint roughness and dilation. Probabilistic approaches, such as Monte Carlo Simulation (MCS), provide useful statistical insight but require extensive site-specific data and probability distributions that are rarely available for existing old dams.

This work presents an Interval Finite Element Method (IFEM) framework for sliding stability assessment under parameter uncertainty. The method integrates interval arithmetic with the nonlinear Barton–Choubey (BC) shear strength model, an element-by-element assembly strategy to reduce dependency effects, and an interval crack initiation and propagation criterion driven by tensile- and shear-stress conditions. External load (uplift pressure) and boundary conditions are updated iteratively as the crack propagates. All uncertain parameters, including Young's modulus, density, Barton-Choubey shear strength parameters, are expressed as intervals and incorporated into the IFEM framework.

The framework is validated through a concrete gravity dam case study using laboratory data, historical temperature records, and construction photographs. Results show that the dam remains stable with interval safety factors consistently above unity and crack lengths closely matching Monte Carlo Simulation (MCS) predictions, while avoiding the excessive safety margins characteristic of LEM. The proposed IFEM approach provides reliable, computationally feasible, and data-efficient safety bounds suitable for dams with limited site information.

Keywords: Concrete gravity dams, Stability, Mohr-Coulomb, Barton-Choubey, Rock joint shear strength, Uncertainty, Interval Finite Element Method, Crack-Based Limit Equilibrium Method, Monte Carlo Simulation, Dam Safety

1. Introduction

Concrete gravity dams resist hydrostatic, uplift, hydrodynamic, silt, thermal, and seismic loads primarily through self-weight and shear resistance mobilized along the concrete–foundation rock interface. Sliding stability along the base represents one of the governing limit states evaluated in dam safety assessments (FERC, 2016; USACE, 2005). Reliable evaluation of sliding resistance requires realistic modeling of interface shear strength and explicit treatment of uncertainty in material properties and loading conditions.

Traditional crack-based Limit Equilibrium Methods (LEM) typically employ linear Mohr–Coulomb (MC) shear strength assumptions. However, laboratory and field investigations demonstrate that rock joint shear strength is nonlinear and stress-dependent due to surface roughness and dilation effects (Barton and Choubey, 1977). Linear MC models may therefore misrepresent sliding resistance, particularly when cracking and uplift redistribution reduce effective normal stress.

Probabilistic approaches such as Monte Carlo Simulation (MCS) propagate uncertainty through repeated sampling of random variables. Although statistically rigorous, these methods require defensible probability distributions, which are rarely available for aging dams. Interval analysis provides an alternative uncertainty framework that does not require probability distributions (Moore, 1979; Muhanna and Mullen, 2001). The Interval Finite Element Method (IFEM) computes guaranteed bounds on structural response under bounded epistemic uncertainty (Muhanna et al., 2007; Yadav, 2025).

This study presents an application-focused comparison of deterministic LEM, Monte Carlo Simulation, and IFEM for sliding stability assessment of a concrete gravity dam under parameter uncertainty. Unlike previous applications of IFEM that assume uniform interval material properties, The present work integrates the nonlinear Barton–Choubey (BC) shear strength model into a two-dimensional interval finite element framework, with a spatially varying elastic modulus that accounts for moisture-dependent stiffness variations. The formulation further couples uplift redistribution and crack propagation, enabling guaranteed safety bounds without assuming probability distributions or relying on resultant-force simplifications inherent in LEM.

2. Methodology

This section presents the governing formulations and computational procedures adopted in the deterministic crack-based Limit Equilibrium Method (LEM), Monte Carlo Simulation (MCS), and Interval Finite Element Method (IFEM) frameworks for sliding stability assessment of concrete gravity dams under parameter uncertainty. While LEM employs the linear Mohr–Coulomb (MC) shear strength model, both MCS and IFEM utilize the nonlinear Barton–Choubey (BC) model to represent the concrete–foundation rock interface behavior. The factor of safety against sliding (FSS) is evaluated in each framework along the sliding interface. The resulting formulations establish the basis for the numerical implementation in Section 3 and the comparative evaluation presented in Section 4.

2.1 Deterministic Crack-Based Limit Equilibrium Method

The deterministic sliding stability assessment follows the crack-based Limit Equilibrium Method formulation presented in Yadav (2025), consistent with current dam safety practice (FERC, 2016; USACE, 2005). The overall analysis procedures are presented below.

2.1.1 External Loads

The governing external loads considered in this study are dead load (self-weight), hydrostatic forces acting on the upstream and downstream faces, and uplift pressure along the sliding interface. Although concrete gravity dams may be subjected to additional loads such as silt loads, hydrodynamic loads, thermal loads, and seismic forces, the overall analytical procedure remains the same as presented in this paper.

The dead load or self-weight is a major stabilizing force and acts vertically downward through the centroid of the dam cross-section (U.S. Army Corps of Engineers 2005, Federal Energy Regulatory Commission 2016). It is computed as:

$$\mathrm{F_D} = \mathrm{V_c}\gamma_\mathrm{c} \tag{1}$$

where $\mathrm{F_D}$ is the dead load or self-weight of dam, $\mathrm{V_c}$ is the volume of concrete, and γ_c is the unit weight of concrete.

Hydrostatic pressure acts perpendicular to the dam face and increases linearly with depth, producing a triangular pressure distribution (De Sazilly 1853, United State Bureau of Reclamation 1987, White 2011). For a vertical surface, the resultant hydrostatic force is given by:

$$\mathrm{F_h} = \frac{1}{2}\gamma_\mathrm{w}\mathrm{h}^2 \tag{2}$$

where $\mathrm{F_h}$ is the hydrostatic force, γ_w is the unit weight of water, and h is the depth of water.

The unit weight of water is taken as $\gamma_\mathrm{w} = 9.81\ \mathrm{kN/m^3}\ (62.4\ \mathrm{lbf/ft^3})$, in accordance with standard engineering practice(United State Bureau of Reclamation 1987, White 2011). The resultant force acts at one-third of the water height measured from the base. Figure 1 and 2 illustrates the dead load acting through C.G, the hydrostatic pressure distribution and corresponding resultant force locations for both upstream and downstream faces.

Uplift pressure is a critical vertical force that reduces the effective compressive normal stress along the concrete–foundation rock interface and directly influences sliding stability (U.S. Army Corps of Engineers 2005, Federal Energy Regulatory Commission 2016, Nallanathel, Ramesh et al. 2018). For an uncracked interface, uplift pressure is commonly assumed to vary linearly from the heel to the toe (Federal Energy Regulatory Commission 2016), as depicted in Figure 1. When cracking occurs, the uplift pressure is assumed to remain constant from the heel to the crack tip and is taken as equal to the headwater pressure, since water can freely enter the crack, followed by a linear decrease to the toe (Federal Energy Regulatory Commission 2016), as depicted in Figure 2.

Because the uplift distribution depends on crack length, and crack length itself depends on the applied loads and resulting stress state, crack-based LEM requires an iterative uplift–crack coupling procedure to obtain a consistent solution (Federal Energy Regulatory Commission 2016).

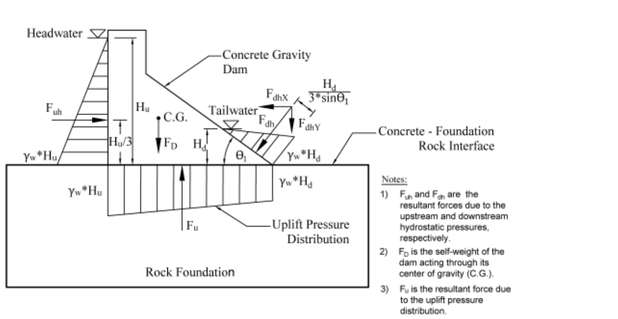

Figure 1: Uplift pressure distribution for an uncracked interface

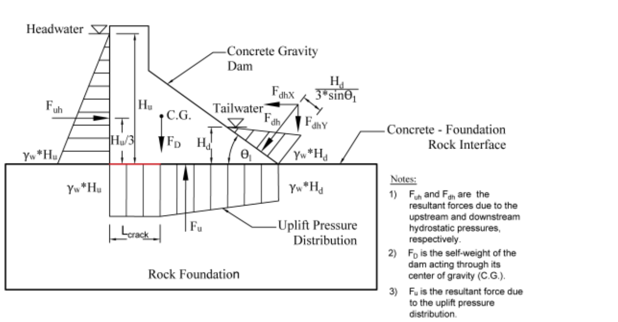

Figure 2: Uplift pressure distribution for a cracked interface

2.1.2 Failure Criterion Utilized in Limit Equilibrium Method (LEM)

In dam stability analysis, establishing a failure criterion is fundamental. The Limit Equilibrium Method (LEM) evaluates stability by assuming the dam is at a limit state, i.e., on the verge of failure (Ali, Alam et al. 2012). At this state, the system satisfies static equilibrium under applied loads, meaning driving and resisting forces and moments are balanced. The term "Limit" denotes the condition immediately preceding failure, while "Equilibrium" implies that all external forces and moments are in balance (Ali, Alam et al. 2012). The dam is treated as a rigid body without deformation, and equilibrium equations are used to compute the factor of safety against sliding (FSS).

A key step in LEM is estimating the shear strength parameters along the concrete–foundation rock interface, namely the friction angle (ϕ) and cohesion (c). For practical application, LEM adopts the linear Mohr–Coulomb (MC) shear strength model, assuming a smooth failure surface. The shear strength is expressed as (Weijermars 1997, Fell, MacGregor et al. 2015):

$$\tau_s = c + \sigma_n \tan\phi \tag{3}$$

where τ_s is the shear strength, c is cohesion, σ_n is the effective compressive normal stress on the sliding plane, and ϕ is the available friction angle.

Based on the known external forces and shear strength parameters, the factor of safety against sliding (FSS) is computed as (Fell, MacGregor et al. 2015):

$$\mathrm{FSS} = \frac{cA_C + A_c\sigma_n \tan\phi}{F_s} \tag{4}$$

where A_C is uncracked area under compression along the concrete-foundation rock interface and F_s is total driving or sliding force along the interface, typically taken as the horizontal component of the resultant load vector.

Due to uncertainty in cohesion, particularly at concrete–rock interfaces, the Federal Energy Regulatory Commission recommends either neglecting cohesion or applying a higher factor of safety (Federal Energy Regulatory Commission 2016). If cohesion is neglected, Equation (4) reduces to:

$$\mathrm{FSS} = \frac{A_c\sigma_n \tan\phi}{F_s} = \frac{\tan\phi}{\frac{F_s}{A_c\sigma_n}} = \frac{\tan\phi}{\tan\alpha_r} \tag{5}$$

where α_r is required friction angle, defined as angle between the resultant load vector and the normal to the sliding plane.

2.1.3. Crack Initiation and Propagation Criteria. In conventional crack-based Limit Equilibrium Method (LEM), the concrete–foundation rock interface is assumed to have zero tensile strength (Federal Energy Regulatory Commission 2016). Any portion of the interface subjected to tensile normal stress is therefore considered cracked.

For illustration, consider the case shown in Figure 3. The base length of the dam is B_0 and B_1 the location of the resultant force measured from the toe. If the resultant lies within the middle third of the base length i.e., between $\frac{B_0}{3}$ and $\frac{2B_0}{3}$, the entire interface remains in compression and no cracking occurs. If the resultant lies outside the middle third, tensile stress develops at the heel and cracking initiates (Federal Energy Regulatory Commission 2016).

For a unit width of the dam section, the normal stresses at the heel and toe are expressed as

$$\sigma_{toe/heel} = \frac{F_{RY}}{B_0} \pm \frac{6F_{RY}e}{{B_0}^2} \tag{6}$$

where F_{RY} is the vertical component of the resultant force and e is the eccentricity measured from the centerline of the base.

When tensile stress develops at the heel, the portion of the interface remaining in compression extends a distance $3B_1$ from the toe, consistent with the triangular stress distribution. The crack length for the first iteration is therefore will be $B_0 - 3B_1$. Figure 3 illustrates the stress distribution corresponding crack length definition along the base interface.

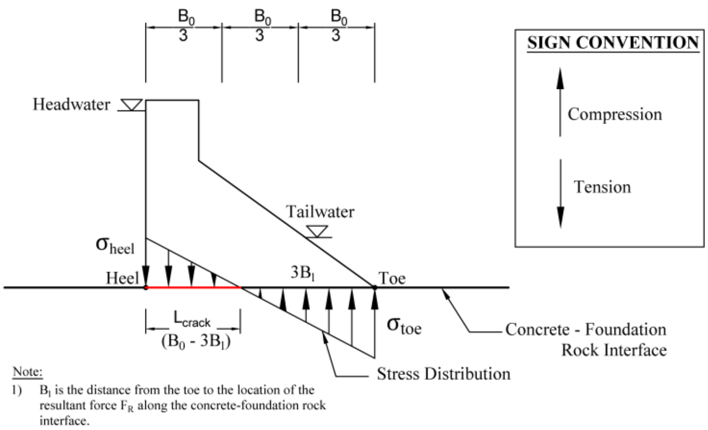

Figure 3: Tension at the heel when resultant force (F_R) is located within the outer third of base length

2.1.4. Iterative Crack–based Solution Procedure

Because the uplift pressure is directly influenced by the extent of cracking, and the crack length is in turn controlled by the applied external loads, its evaluation requires an iterative procedure. This interdependence forms the basis of the crack–based LEM(Federal Energy Regulatory Commission 2016). Accordingly, crack–based LEM requires determining the crack length along the sliding interface, followed by an evaluation of stability against sliding.

2.1.4.1 Crack Length Determination

The determination of crack length follows these steps:

a) **Initial Assumption:** The interface has zero tensile strength. Assume no initial crack and apply the uplift pressure distribution for a non-cracked base, as discussed in Section 2.1.3.
b) **Determine Resultant Force Location:** Find the location of the resultant force by taking moments about the heel or toe. Let B_0, be the base length of dam and B_1 be the resultant force location from the toe.
c) **Compute Compression Zone:** The portion of base under compression will be $3B_1$ from the toe.
d) **Check the Compression Condition:**
   - If $3B_1 \geq B_0$, the entire base is in compression. Hence there will be no cracking. Assumed uplift pressure distribution is correct and proceed to factor of safety against sliding (FSS) computation as described in Section 2.1.5.

- If $3B_1 < B_0$, the entire base is not in compression. Hence there will be cracking, and the new crack length will be $Lc = B_0 - 3B_1$.

e) **Re-apply uplift pressure:** If there is cracking, update the uplift pressure distribution for the cracked base, based on the calculated crack length, as discussed in Section 2.1.3.

f) **Recalculate Resultant Force Location:** Determine the new location of resultant force, B_1, from the toe by taking moments about the heel or toe.

g) **Update Crack Length:** Compute the new crack length: $Lc\_new = B_0 - 3B_1$.

h) **Iterate Until Convergence:** Repeat steps e to g until the crack length converges or until the entire base is cracked. If the entire base is cracked, the dam is considered unstable and will undergo sliding unless the sufficient anchoring measures are implemented to satisfy current engineering guidelines. If the entire base is not cracked, proceed with steps outlined in Section 2.1.5.

2.1.5 Factor of Safety against Sliding (FSS)

Once the crack length and corresponding uplift forces are determined, the magnitude and location of the new resultant force (F_R) along the sliding interface are calculated by taking moments about the heel or toe of the dam. From the components of the resultant force, the required friction angle (α_r) with respect to the normal to the sliding plane is obtained as:

$$\alpha_r = \tan^{-1}\left|\frac{F_{RX}}{F_{RY}}\right| \tag{7}$$

where F_{RX} and F_{RY} are the horizontal and vertical components of the resultant force, respectively.

The available friction angle (ϕ) is selected based on the foundation rock type. The factor of safety against sliding (FSS) is then computed using Equation (5).

Sliding stability is satisfied when $FSS \geq 1$, i.e., when the available friction angle (ϕ) exceeds or equals the required friction angle (α_r). If $FSS < 1$, the dam is considered unstable with respect to sliding and may require anchoring or other stabilization measures to meet current engineering guidelines.

2.2 Failure Criterion Utilized in Monte Carlo Simulation (MCS) and Interval Finite Element Method (IFEM)

In the 1970s, Barton introduced his initial non-linear shear strength criterion for rock joints, utilizing the basic friction angle (ϕ_b), derived from an analysis of joint strength data available in the literature. Later, Barton and Choubey (1977) refined this equation based on their direct shear test results conducted on 130 samples of rock joints with varying degrees of weathering, leading to a revised formulation as shown in Equation (8).

$$\tau_s = \sigma_n \tan\left(\phi_r + \mathrm{JRC}\log_{10}\left(\frac{\mathrm{JCS}}{\sigma_n}\right)\right) \tag{8}$$

where ϕ_r is residual friction angle in degree, JRC is the joint roughness coefficient and JCS is the join wall compressive strength.

2.3 Monte Carlo Simulation (MCS)

The Monte Carlo simulation (MCS) is implemented to evaluate variability in sliding stability due to uncertain parameters. The uncertain parameters include the density of concrete, the unit weight of water, the joint roughness coefficient (JRC), the joint wall compressive strength (JCS), and the residual friction angle (ϕ_r).. These parameters are defined using the same interval bounds adopted in IFEM to ensure consistency. Sampling is performed using scaled Beta distributions, bounded on the interval $[\underline{X}, \overline{X}]$. The mean value ($X_{mean}$) is taken as the midpoint of the interval, and the shape parameters of the scaled Beta distribution are obtained as:

$$\alpha_{MCS} = \mu_{MCS}\kappa, \qquad \beta_{MCS} = (1 - \mu_{MCS})\kappa \quad (9) \qquad\qquad \mu_{MCS} = \frac{(X_{mean} - \underline{X})}{(\overline{X} - \underline{X})} \quad (10)$$

where α_{MCS} and β_{MCS} are the Beta shape parameters, μ_{MCS} defines the scaled location of the mean within the interval, and κ is the concentration factor controlling the spread of the realizations around the mean.

The probability density function of the Beta distribution used for sampling is expressed as:

$$f(x) = \frac{x^{\alpha_{MCS}-1}(1-x)^{\beta_{MCS}-1}}{\mathrm{Beta}(\alpha_{MCS}, \beta_{MCS})} \quad (11) \qquad \mathrm{Beta}(\alpha_{MCS}, \beta_{MCS}) = \int_0^1 n^{\alpha_{MCS}-1}(1-n)^{\beta_{MCS}-1}dn \quad (12)$$

where x is the sampled random variable and n is a dummy integration variable.

A concentration factor (κ) is selected based on the expected variability of each uncertain parameter. Higher κ values (e.g., for densities) yield narrower distributions around the mean, whereas moderate κ values (e.g., for JRC, JCS and ϕ_r) allow a broader spread across the full interval of each parameter. The resulting realizations are then propagated through the uplift–crack coupling formulation to compute the crack length and factor of safety for each simulation.

The severity of cracking is coupled to the Barton–Choubey shear strength model. First, the uplift distribution assuming no crack is taken as a trapezoid:

$$F_{u0} = \frac{1}{2}(\gamma_w H_u + \gamma_w H_d) B_0 \tag{13}$$

where F_{u0} is the uplift force, H_u is the headwater depth, H_d is the tailwater depth, B_0 is the dam base length and γ_w is the unit weight of water.

The effective pre-crack normal stress is calculated as:

$$\sigma_0 = \max\left(\frac{F_D - F_{u0}}{B_0}, 0\right) \tag{14}$$

where F_D is the self-weight of dam and the corresponding mobilized friction angle was given by:

$$\phi_{BC} = \phi_r + \mathrm{JRC}\log_{10}\left(\frac{\mathrm{JCS}}{\sigma_0}\right) \tag{15}$$

A severity index (s_0) is then defined as:

$$s_0 = \frac{F_s}{F_s + \tan\phi_{BC}\max(F_D - F_{u0}, 1)} \tag{16}$$

where F_s is the sliding force.

A severity index (s_0) links crack length to the balance between sliding force and mobilized BC shear resistance. When the sliding force dominates, s_0 is larger and longer cracks are promoted, whereas when resistance is higher, s_0 is smaller and the crack is shorter. This coupling ensures that the crack length distribution is not imposed arbitrarily but responds directly to the mobilized shear strength. The actual crack length (Lc) was sampled from a Beta distribution whose mean was tied to s_0 as:

$$\mathrm{Lc} = B_0\left(\mathrm{Beta}\big(1 + \lambda_{LC}s_0, 1 + \lambda_{LC}(1 - s_0)\big)\right) \tag{17}$$

where beta concentration factor (λ_{LC}) is set above 20 to maintain concentration around the mean. The adopted Beta-based crack length sampling is not imposed arbitrarily; rather, its mean is tied to severity index (s_0) ensuring that crack propagation responds directly to the mobilized shear strength and applied sliding demand.

Uplift after cracking is taken as:

$$F_u = \gamma_w H_u \mathrm{Lc} + \frac{1}{2}(\gamma_w H_u + \gamma_w H_d)(B_0 - \mathrm{Lc}) \tag{18}$$

The normal compressive stress on the bonded portion is calculated as:

$$\sigma_1 = \max\left(\frac{F_D - F_{u0}}{B_0 - \mathrm{Lc}}, \sigma_{floor}\right) \tag{19}$$

where σ_{floor} is set to 1 Pa for numerical safeguard.

The Barton–Choubey friction angle is then re-evaluated at the bonded interface as:

$$\phi_{BC} = \phi_r + \mathrm{JRC}\log_{10}\left(\frac{\mathrm{JCS}}{\sigma_1}\right) \tag{20}$$

Since MCS does not discretize the interface, shear strength is evaluated through angle comparison. The resultant of the sliding and vertical forces makes an angle, α_r, :with respect to the normal to the sliding plane and can be determined as:

$$\alpha_r = \tan^{-1}\left|\frac{F_S}{F_D - F_{u0}}\right| \tag{21}$$

The factor of safety against sliding (FSS) is computed as:

$$\mathrm{FSS} = \frac{\tan\phi_{BC}}{\tan\alpha_r} \tag{22}$$

This expression tests whether the mobilized Barton–Choubey shear strength is sufficient to resist the resultant action without making assumptions about the stress distribution along the interface. Unlike IFEM, which integrates the shear strength distribution, the MCS compares mobilized and resultant angles, providing a lumped yet computationally efficient estimate of the factor of safety.

2.4 Interval Finite Element Method (IFEM)

The Interval Finite Element Method (IFEM) is adopted to rigorously propagate uncertainty in material properties, geometry, and external loads through the structural equilibrium equations. Uncertain parameters are represented as interval variables, and the computed solution provides guaranteed bounds that enclose the true structural response. It should be noted that the resulting uncertainty bounds are mesh-dependent, as they are influenced by the level of discretization and the associated approximation of the structural domain. An introduction to interval arithmetic, with relevant discussions can be found in (Moore 1966, Kulisch 1981, Alefeld 1983, Neumaier 1990), along with an overview of the main computational challenges such as dependency and overestimation.

Hereafter, boldface font is used to denote interval quantities.

The structural equilibrium is defined through the interval linear system:

$$\mathbf{K}\mathbf{u} = \mathbf{f} \tag{23}$$

where $\mathbf{K}$ is the interval global stiffness matrix, $\mathbf{u}$ is the interval nodal displacement vector, and $\mathbf{f}$ is the interval equivalent nodal load vector.

Derived quantities are obtained as:

$$\boldsymbol{\varepsilon} = \mathrm{B}\mathbf{u}, \qquad \boldsymbol{\sigma} = \mathbf{S}\mathbf{u} \tag{24}$$

where B is the strain–displacement matrix and $\mathbf{S}$ is the stress–displacement matrix.

2.4.1 Decomposition of the Stiffness and Stress Matrices

To minimize dependency-induced overestimation in interval arithmetic, the stiffness matrix is decomposed as:

$$\mathbf{K} = \mathrm{A}\mathrm{diag}(\Lambda\boldsymbol{\alpha})\mathrm{A}^{\mathrm{T}} \tag{25}$$

where A and Λ are deterministic matrices, $\boldsymbol{\alpha}$ is the interval parameter vector.

For an 8-node rectangular isoparametric element under plane stress or strain conditions, the Young's modulus $(\mathbf{E})$ is represented as an interval. The corresponding stiffness matrix is then calculated as:

$$\mathbf{K_e} = \int_{\Omega} \mathrm{B}_{\mathrm{e}}^{\mathrm{T}}(\xi)\mathbf{E_e}(\xi)\mathrm{B}_{\mathrm{e}}(\xi)\mathrm{t}(\xi)\mathrm{d}\Omega \tag{26}$$

where t is the thickness and $\mathrm{B_e}$ is the strain-displacement matrix.

The integral in Equation (26) is typically evaluated using a 3 × 3 Gaussian quadrature rule:

$$\mathbf{K_e} = \sum_{\mathrm{j}=1}^{9} \mathrm{B}_{\mathrm{e}}^{\mathrm{T}}(\xi_{\mathrm{j}})\mathbf{E_e}(\xi_{\mathrm{j}})\mathrm{B}_{\mathrm{e}}(\xi_{\mathrm{j}})\mathrm{w_j}\mathrm{J}(\xi_{\mathrm{j}})\mathrm{t}(\xi) \tag{29}$$

where, $\mathrm{w_j}$ are weights at the integration points, ξ_{j} is the integration coordinate, and J is the determinant of the Jacobian matrix for the transformation from local to global coordinates. This numerical integration transforms the modulus field into a smoother interval representation.

The constitutive matrix $\mathbf{E_e}(\xi_{\mathrm{j}})$ in Equation (29) can be expressed as:

$$\mathbf{E_e}(\xi_{\mathrm{j}}) = \Phi_{\mathrm{e}}\mathrm{diag}\{\phi_e\mathbf{E}_{\mathrm{j}}\}\Phi_{\mathrm{e}}^{\mathrm{T}} \tag{30}$$

where Φ_{e} is a 3 × 3 deterministic matrix whose columns are eigenvectors ϕ_e is a 3 × 1 vector whose rows are eigenvalues. Both Φ_{e} and ϕ_e depends on Poisson's ratio (ν), and $\mathbf{E}_{\mathrm{j}}$ is the Young's modulus at j-th integration point ξ_{j}. Using this, Equation (29) becomes:

$$\begin{aligned}\mathbf{K_e} &= \sum_{\mathrm{j}=1}^{9} \mathrm{B}_{\mathrm{e}}^{\mathrm{T}}(\xi_{\mathrm{j}})\Phi_{\mathrm{e}}\mathrm{diag}\{\phi_e\mathbf{E_j}\}\Phi_{\mathrm{e}}^{\mathrm{T}}\mathrm{B}_{\mathrm{e}}(\xi_{\mathrm{j}})\mathrm{w_j}\mathrm{J}(\xi_{\mathrm{j}})\mathrm{t}(\xi) \\ &= \{\mathrm{B}_{\mathrm{e}}^{\mathrm{T}}(\xi_1)\Phi_{\mathrm{e}} \dots\dots\dots\dots. \mathrm{B}_{\mathrm{e}}^{\mathrm{T}}(\xi_9)\Phi_{\mathrm{e}}\}\end{aligned} \tag{31}$$

$$\begin{Bmatrix} (w_1 J_1 t_1)\mathrm{diag}(\phi_e)\mathbf{E_1} & & \\ & \ddots & \\ & & (w_9 J_9 t_9)\mathrm{diag}(\phi_e)\mathbf{E_9} \end{Bmatrix} \begin{Bmatrix} \Phi_e^T B_e(\xi_1) \\ \vdots \\ \Phi_e^T B_e(\xi_9) \end{Bmatrix}$$

where the subscripts j denotes quantities at the j-th integration point. The deterministic matrices A_e and Λ_e are obtained as:

$$A_e = \{B_e^T(\xi_1)\Phi_e \ldots\ldots\ldots\ldots B_e^T(\xi_9)\Phi_e\};$$

$$\Lambda_e = \begin{Bmatrix} (w_1 J_1 t_1)\mathrm{diag}(\phi_e) & & \\ & \ddots & \\ & & (w_9 J_9 t_9)\mathrm{diag}(\phi_e) \end{Bmatrix}, \qquad \boldsymbol{\alpha}_\mathbf{e} = \begin{Bmatrix} \mathbf{E_1} \\ \vdots \\ \mathbf{E_9} \end{Bmatrix} \tag{32}$$

This decomposition of the diagonal matrix, $\mathrm{diag}(\Lambda_e \boldsymbol{\alpha}_\mathbf{e})$, effectively reduces redundant interval terms and plays a critical role in reducing overestimation in interval due to dependency.

The element stress-displacement matrix ($\mathbf{S_e}$) depends linearly on the stiffness parameter vector $\boldsymbol{\alpha}_\mathbf{e}$. Just like the stiffness matrix $\mathbf{K_e}$, this matrix ($\mathbf{S_e}$) can also be expressed in a simplified and structured form. The matrix $\mathbf{S_e}$ is written as:

$$\mathbf{S_e} = \Phi_{se}\mathrm{diag}(\Lambda_{se}\boldsymbol{\alpha}_\mathbf{e})A_{se}^T \tag{33}$$

For example, at any location within 8-node rectangular isoparametric element, the stress $\boldsymbol{\sigma}_\mathbf{e}$ can be obtained either by interpolating or extrapolating the stresses calculated at the integration (Gauss) points. This procedure is described by:

$$\boldsymbol{\sigma}_\mathbf{e} = \sum_{j=1}^{9} \upsilon_j \boldsymbol{\sigma}_\mathbf{e}(\xi_j) = \sum_{j=1}^{9} \upsilon_j\, \mathbf{E_e}(\xi_j) B_e(\xi_j)\mathbf{u_e} \tag{34}$$

where ξ_j represents the coordinates of the numerical integration points, υ_j are the corresponding interpolation or extrapolation weights, and $\mathbf{u_e}$ is the nodal displacement vector of the element. By factoring out $\mathbf{u_e}$, the stress-displacement matrix $\mathbf{S_e}$ takes a simplified form:

$$\mathbf{S}_{\boldsymbol{e}} = \sum_{j=1}^{9} \upsilon_j \mathbf{E_e}(\xi_j) B_e(\xi_j) \tag{35}$$

Substituting $\mathbf{E_e}(\xi_j) = \Phi_e \mathrm{diag}\{\phi_e \mathbf{E}_j\}\Phi_e^T$ into Equation (35):

$$\mathbf{S_e} = \sum_{j=1}^{9} \upsilon_j\, \Phi_e \mathrm{diag}\{\phi_e \mathbf{E}_j\}\Phi_e^T B_e(\xi_j)$$

$$= \{\Phi_e \ \cdots \ \Phi_e\} \begin{Bmatrix} \upsilon_1 \mathrm{diag}(\phi_e)\mathbf{E}_1 & & \\ & \ddots & \\ & & \upsilon_9 \mathrm{diag}(\phi_e)\mathbf{E}_9 \end{Bmatrix} \begin{Bmatrix} \Phi_e^T B_e(\xi_1) \\ \vdots \\ \Phi_e^T B_e(\xi_9) \end{Bmatrix} \tag{36}$$

The deterministic matrices Φ_{se}, Λ_{se} and A_{se} are obtained as:

$$\Phi_{se} = \{\Phi_e \ \cdots \ \Phi_e\}, \qquad \Lambda_{se} = \begin{Bmatrix} \upsilon_1 \mathrm{diag}(\phi_e) & & \\ & \ddots & \\ & & \upsilon_9 \mathrm{diag}(\phi_e) \end{Bmatrix};$$

$$A_{se} = \{{B_e}^T(\xi_1)\Phi_e \quad \ldots \quad {B_e}^T(\xi_9)\Phi_e\} \tag{37}$$

These decompositions are performed at the element level before global assembly using an Element-by-Element (EBE) strategy.

2.4.2 Decomposition of Equivalent Nodal Load Vector

For an element subjected to concentrated, body, and line loads, the uncertain load vector is expressed as:

$$\delta = [\mathbf{P_c} \quad \mathbf{P_s} \quad \mathbf{P_l}]^T \tag{38}$$

The equivalent nodal load vector becomes:

$$\mathbf{f} = F\delta \tag{39}$$

where F is a deterministic matrix constructed from shape functions and Jacobian terms.

2.4.3 Matrix Assembly – Element–by–Element (EBE)

After determining the element-level matrices, $\mathbf{K}_e$ (stiffness matrix), $\mathbf{f}_e$ (nodal load vector), $\mathbf{S}_e$ (stress–displacement matrix), and B_e (strain–displacement matrix), these must be assembled to form their global counterparts: **K**, **f**, **S**, and B.

This is accomplished using the Element-by-Element (EBE) approach, which assembles each matrix in a block-by-block manner (Muhanna, Zhang et al. 2007, Mallella, Mullen et al. 2011, Muhanna, Mallela et al. 2013, Xiao 2015). In this method, the entire structure is modeled as a collection of separate elements connected by shared nodes. The global displacement vector $\mathbf{u}$ is formed by combining all local element displacement vectors $\mathbf{u}_e$, with $\mathbf{u}_n$ representing the displacement vector of the common (shared) nodes. Consequently, the global stiffness matrix **K** and global nodal load vector **f** are assembled from their element counterparts as shown in Equation (40):

$$\mathbf{u} = \begin{Bmatrix} \mathbf{u_e} \\ \vdots \\ \mathbf{u_e} \\ \mathbf{u_n} \end{Bmatrix}, \quad \mathbf{K} = \begin{Bmatrix} \mathbf{K_e} & & \\ & \ddots & \\ & & \mathbf{K_e} \\ 0 & & 0 \end{Bmatrix}, \quad \mathbf{f} = \begin{Bmatrix} \mathbf{f_e} \\ \vdots \\ \mathbf{f_e} \\ \mathbf{f_n} \end{Bmatrix} \tag{40}$$

where $\mathbf{f}_n$ represents the concentrated loads directly applied to the common nodes. Unlike standard FEM assembly, where the global matrices are formed in a single step, the EBE method constructs **K** and **f** by stacking individual $\mathbf{K}_e$ and $\mathbf{f}_e$ blocks. One key point to note is that the global stiffness matrix **K** is initially singular since it does not yet incorporate constraints such as boundary conditions.

To reduce overestimation due to dependency from repeated interval variables, the matrices **K** and **f** are further decomposed using interval decomposition techniques $\mathbf{K} = \mathrm{A}\mathrm{diag}(\Lambda\alpha)\mathrm{A}^{\mathrm{T}},\ \mathbf{f} = \mathrm{F}\delta$, as follows:

$$\boldsymbol{\alpha}_\mathbf{e} = \mathrm{L}_\alpha \boldsymbol{\alpha}\,, \quad \boldsymbol{\delta}_\mathrm{e} = \mathrm{L}_\delta \boldsymbol{\delta} \tag{41}$$

In this representation, $\boldsymbol{\alpha}_\mathrm{e}$ and $\boldsymbol{\delta}_\mathrm{e}$ (element-level interval vectors) are either selected directly from, or interpolated from, the global interval vectors $\boldsymbol{\alpha}$ and $\boldsymbol{\delta}$. These element-level vectors are related to the global ones through mapping relations:

The global matrices A, Λ, and F are assembled in a way similar to **K** and **f**, again using a block-by-block strategy:

$$\mathrm{A} = \begin{Bmatrix} \mathrm{A_e} & & \\ & \ddots & \\ & & \mathrm{A_e} \\ 0 & & 0 \end{Bmatrix}, \quad \Lambda = \begin{Bmatrix} \Lambda_\mathrm{e}\mathrm{L}_\alpha \\ \vdots \\ \Lambda_\mathrm{e}\mathrm{L}_\alpha \end{Bmatrix}, \quad \mathrm{F} = \begin{Bmatrix} \mathrm{F_e}\mathrm{L}_\delta \\ \vdots \\ \mathrm{F_e}\mathrm{L}_\delta \\ \mathrm{F_n} \end{Bmatrix} \tag{42}$$

where $\mathbf{f}_\mathrm{n} = \mathrm{F}_\mathrm{n}\boldsymbol{\delta}$ is the decomposition of $\mathbf{f}_\mathrm{n}$. If any interval components in $\boldsymbol{\alpha}$ or $\boldsymbol{\delta}$ refer to the same variable, the corresponding columns in Λ or F must be summed. Similarly, if certain components in $\boldsymbol{\delta}$ are zero, the associated columns in F are removed to avoid redundancy.

The global strain vector $\boldsymbol{\varepsilon}$ is assembled by combining all the element-level strain vectors $\boldsymbol{\varepsilon}_e$. The global strain-displacement matrix B is also constructed in block using each element matrix $\mathrm{B_e}$. This assembly procedure ensures that all local contributions are consistently represented in the global system, preparing it for further analysis:

$$\boldsymbol{\varepsilon} = \begin{Bmatrix} \boldsymbol{\varepsilon}_\mathrm{e} \\ \vdots \\ \boldsymbol{\varepsilon}_\mathrm{e} \end{Bmatrix}, \quad \mathrm{B} = \begin{Bmatrix} \mathrm{B_e} & & 0 \\ & \ddots & \vdots \\ & \mathrm{B_e} & 0 \end{Bmatrix} \tag{43}$$

$$\boldsymbol{\sigma} = \begin{Bmatrix} \boldsymbol{\sigma}_\mathrm{e} \\ \vdots \\ \boldsymbol{\sigma}_\mathrm{e} \end{Bmatrix}, \quad \mathbf{S} = \begin{Bmatrix} \mathbf{S_e} & & 0 \\ & \ddots & \vdots \\ & \mathbf{S_e} & 0 \end{Bmatrix} \tag{44}$$

Finally, the deterministic matrices Φ_s, Λ_s and $\mathrm{A_s}$ are assembled as:

$$\Phi_\mathrm{s} = \begin{Bmatrix} \Phi_\mathrm{se} & & \\ & \ddots & \\ & & \Phi_\mathrm{se} \end{Bmatrix}, \quad \Lambda_\mathrm{s} = \begin{Bmatrix} \Lambda_\mathrm{se}\mathrm{L}_\alpha \\ \vdots \\ \Lambda_\mathrm{se}\mathrm{L}_\alpha \end{Bmatrix}, \quad \mathrm{A_s} = \begin{Bmatrix} \mathrm{A_{se}} & & \\ & \ddots & \\ & & \mathrm{A_{se}} \\ 0 & \dots & 0 \end{Bmatrix} \tag{45}$$

2.4.4 Calculation of reactions and derived variables ($\boldsymbol{\varepsilon}$ and $\boldsymbol{\sigma}$)

After the global stiffness matrix **K** is assembled using the EBE strategy, it remains singular. This occurs because, at this stage, the model does not yet include connections between shared nodes of adjacent elements, nor are essential boundary conditions applied. As a result, the assembled system lacks the necessary constraints to produce a unique solution.

To resolve this, both compatibility requirements and essential boundary conditions must be enforced. These constraints are expressed in the form of a matrix equation $\mathrm{C}\mathbf{u} = 0$, where C is a constraint matrix that enforces physical conditions, such as continuity between nodes and essential boundary conditions. Once these conditions are imposed, the singularity of the stiffness matrix is eliminated, and the system becomes fully solvable.

As an example, consider an 8-node rectangular isoparametric element, where each node has two degrees of freedom. To enforce compatibility between an element node (with two DOFs) and a corresponding common node using a constraint matrix C, the two rows of C can be defined as in Eq. (46) (Mallella, Mullen et al. 2011, Xiao 2015):

$$\begin{array}{cc} & \text{Element node DOF} \quad \text{Common node DOF} \\ \mathrm{C} = & \left\{\begin{array}{cccc|ccc} \cdots & \cdots & \cdots & \cdots & \cdots & \cdots & \cdots \\ \cdots & 1 & 0 & \cdots & -1 & 0 & \cdots \\ \cdots & 0 & 1 & \cdots & 0 & -1 & \cdots \\ \cdots & \cdots & \cdots & \cdots & \cdots & \cdots & \cdots \end{array}\right\} \end{array} \quad (46)$$

$$\begin{array}{cc} & \text{Element node DOF} \quad \text{Common node DOF} \\ \mathrm{C} = & \left\{\begin{array}{cccc|ccc} \cdots & \cdots & \cdots & \cdots & \cdots & \cdots & \cdots \\ \cdots & 0 & 0 & \cdots & 1 & 0 & \cdots \\ \cdots & 0 & 0 & \cdots & 0 & 1 & \cdots \\ \cdots & \cdots & \cdots & \cdots & \cdots & \cdots & \cdots \end{array}\right\} \end{array} \quad (47)$$

To apply essential boundary conditions, specific entries in the constraint matrix C are assigned a value of 1, while other entries in the same row are set to zero as in Eq. (47) (Mallella, Mullen et al. 2011, Xiao 2015).

To enforce these compatibility conditions and maintain equilibrium, a Lagrange multiplier $\boldsymbol{\lambda}$ is introduced. The system's energy functional, $\boldsymbol{\Pi}$, is given by:

$$\boldsymbol{\Pi} = \frac{\mathbf{1}}{\mathbf{2}}\mathbf{u}^{\mathrm{T}}\mathbf{K}\mathbf{u} - \mathbf{u}^{\mathrm{T}}\mathbf{f} + \lambda^{\mathrm{T}}\mathrm{C}\mathbf{u} \qquad (48)$$

By minimizing $\boldsymbol{\Pi}$ with respect to $\mathbf{u}$ and $\boldsymbol{\lambda}$, the interval-based governing equation is obtained:

$$\begin{Bmatrix} \mathbf{K} & \mathrm{C}^{\mathrm{T}} \\ \mathrm{C} & 0 \end{Bmatrix} \begin{Bmatrix} \mathbf{u} \\ \lambda \end{Bmatrix} = \begin{Bmatrix} \mathbf{f} \\ 0 \end{Bmatrix} \qquad (49)$$

To reduce overestimation, the stiffness matrix $\mathbf{K}$ and load vector $\mathbf{f}$ are decomposed as previously described in Equation (25) and (39) respectively. In this formulation, Equation (49) is expressed as (Muhanna, Mallela et al. 2013, Xiao 2015):

$$\begin{Bmatrix} \mathrm{A} \\ 0 \end{Bmatrix} \mathrm{diag}(\Lambda\Delta\boldsymbol{\alpha})\{\mathrm{A}^{\mathrm{T}} \quad 0\} + \begin{Bmatrix} \mathrm{K}_0 & \mathrm{C}^{\mathrm{T}} \\ \mathrm{C} & 0 \end{Bmatrix} \begin{Bmatrix} \mathbf{u} \\ \lambda \end{Bmatrix} = \begin{Bmatrix} \mathrm{F} \\ 0 \end{Bmatrix} \boldsymbol{\delta} \qquad (50)$$

where $\Delta\boldsymbol{\alpha}$ represents the difference between the interval vector $\boldsymbol{\alpha}$ and its reference value α_0, i.e. $\Delta\boldsymbol{\alpha} = \boldsymbol{\alpha} - \alpha_0$, with $\alpha_0 = \mathrm{mid}(\boldsymbol{\alpha})$ being the midpoint value of the interval, and $\mathrm{K}_0 = \mathrm{A}\mathrm{diag}(\Lambda\alpha_0)\mathrm{A}^{\mathrm{T}}$.

The Lagrange multiplier $\boldsymbol{\lambda}$ has physical meaning in this context: it represents internal forces between element nodes and common nodes when compatibility is enforced, and reaction forces at supports when essential boundary conditions are applied. Thus, internal forces and support reactions can be directly obtained as by-products of solving the constraint equation $\mathrm{C}\mathbf{u} = 0$ (Xiao 2015).

Additional derived quantities such as generalized strain ($\boldsymbol{\varepsilon}$) and stress ($\boldsymbol{\sigma}$) in Equation (24) can also be computed. To avoid intermediate interval steps and further overestimation, these variables ($\mathbf{u}, \boldsymbol{\varepsilon},$ and $\boldsymbol{\sigma}$) are solved simultaneously by introducing additional Lagrange multipliers $\boldsymbol{\mu_1}$ and $\boldsymbol{\mu_2}$, corresponding to the relations $\boldsymbol{\varepsilon} = \mathrm{B}\mathbf{u}$ and $\boldsymbol{\sigma} = \mathbf{S}\mathbf{u}$, respectively. The modified energy functional is then expressed as:

$$\boldsymbol{\Pi} = \frac{1}{2}\mathbf{u}^{\mathrm{T}}\mathbf{K}\mathbf{u} - \mathbf{u}^{\mathrm{T}}\mathbf{f} + \lambda^{\mathrm{T}}\mathrm{C}\mathbf{u} + \mu_{\mathbf{1}}^{\mathrm{T}}(\boldsymbol{\varepsilon} - \mathrm{B}\mathbf{u}) + \mu_{\mathbf{2}}^{\mathrm{T}}(\boldsymbol{\sigma} - \mathbf{S}\mathbf{u}) \qquad (51)$$

Above formulation includes six unknowns: $\mathbf{u}, \boldsymbol{\lambda}, \boldsymbol{\mu_1}, \boldsymbol{\mu_2}, \boldsymbol{\varepsilon},$ and $\boldsymbol{\sigma}$. Taking the first variation of this energy functional yields:

$$\begin{Bmatrix} \mathbf{K} & \mathrm{C}^{\mathrm{T}} & \mathrm{B}^{\mathrm{T}} & \mathbf{S}^{\mathrm{T}} & 0 & 0 \\ \mathrm{C} & 0 & 0 & 0 & 0 & 0 \\ \mathrm{B} & 0 & 0 & 0 & -I & 0 \\ \mathbf{S} & 0 & 0 & 0 & 0 & -I \\ 0 & 0 & -I & 0 & 0 & 0 \\ 0 & 0 & 0 & -I & 0 & 0 \end{Bmatrix} \begin{Bmatrix} \mathbf{u} \\ \lambda \\ \boldsymbol{\mu_1} \\ \boldsymbol{\mu_2} \\ \boldsymbol{\varepsilon} \\ \boldsymbol{\sigma} \end{Bmatrix} = \begin{Bmatrix} \mathbf{f} \\ 0 \\ 0 \\ 0 \\ 0 \\ 0 \end{Bmatrix} \qquad (52)$$

From the last two rows of Equation (52), it can be inferred that $\mu_1 = 0$ and $\mu_2 = 0$ Substituting these trivial solutions back into Equation (52) yields a simplified, asymmetric form:

$$\begin{Bmatrix} \mathbf{K} & C^T & 0 & 0 \\ C & 0 & 0 & 0 \\ B & 0 & -I & 0 \\ \mathbf{S} & 0 & 0 & -I \end{Bmatrix} \begin{Bmatrix} \mathbf{u} \\ \boldsymbol{\lambda} \\ \boldsymbol{\varepsilon} \\ \boldsymbol{\sigma} \end{Bmatrix} = \begin{Bmatrix} \mathbf{f} \\ 0 \\ 0 \\ 0 \end{Bmatrix} \tag{53}$$

While this results in a smaller stiffness matrix, it is no longer symmetric (Xiao 2015). Considering the previous decomposition of $\mathbf{K}$ and $\mathbf{f}$, the governing equation can finally be written as (Muhanna, Mallela et al. 2013, Xiao 2015):

$$\begin{Bmatrix} A & 0 \\ 0 & 0 \\ 0 & 0 \\ 0 & \Phi_s \end{Bmatrix} \mathrm{diag}\left(\begin{Bmatrix} \Lambda \\ \Lambda_s \end{Bmatrix} \Delta\boldsymbol{\alpha}\right) \begin{Bmatrix} A^T & 0 & 0 & 0 \\ A_S^T & 0 & 0 & 0 \end{Bmatrix} + \begin{Bmatrix} K_0 & C^T & 0 & 0 \\ C & 0 & 0 & 0 \\ B & 0 & -I & 0 \\ S_0 & 0 & 0 & -I \end{Bmatrix} \begin{Bmatrix} \mathbf{u} \\ \boldsymbol{\lambda} \\ \boldsymbol{\varepsilon} \\ \boldsymbol{\sigma} \end{Bmatrix} = \begin{Bmatrix} F \\ 0 \\ 0 \\ 0 \end{Bmatrix} \boldsymbol{\delta} \tag{54}$$

where $\Delta\boldsymbol{\alpha}$ and K_0 have the same definitions as in Equation (50), and S_0 denotes the generalized stress-displacement matrix as defined earlier, i.e., $S_0 = \Phi_s \mathrm{diag}(\Lambda_s \alpha_0) A_s^T$

Equation (54) can be expressed in a generalized form as:

$$\{A_g \mathrm{diag}(\Lambda_g \Delta\boldsymbol{\alpha}) B_g + K_g\} \mathbf{u_g} = F_g \boldsymbol{\delta} \tag{55}$$

where $A_g, \Lambda_g, B_g, K_g, F_g$ are deterministic matrices, while $\Delta\boldsymbol{\alpha}$ and $\boldsymbol{\delta}$ are interval vectors.

Equations (50) and (54) are the equilibrium equations to be solved. The generalized form of these equations are given in Equation (55). Any interval solver can be employed to solve this general equation. In this paper, a new version of the iterative enclosure method introduced by Xiao (2015) is utilized, which applies an expanding strategy that begins with a simple initial guess and progressively refines the solution.

2.4.5 Piecewise Approach to Reduce Dependency in the Barton–Choubey (BC) Shear Strength Model

Since the BC shear strength model involves uncertain parameters, such as joint roughness coefficient (JRC), joint wall compressive strength (JCS), and residual friction angle (ϕ_r), arising from natural geological variability and site characterization, dependency-induced overestimation can occur in interval computations. To mitigate this effect, this research adopts the piecewise (partition) strategy. The method works as follows:

1) Partition the original uncertain interval **X** into N subintervals:

$$\mathbf{X} = \cup \mathbf{X}^{(i)}\ , \quad \mathbf{X}^{(i)} = \left[\underline{X}^{(i)}, \overline{X}^{(i)}\right], \qquad i = 1 \ldots\ldots N \tag{56}$$

2) Evaluate the interval function $f(\mathbf{X}^{(i)})$ of the function $f(\mathbf{X})$ over each subinterval.
3) Take the hull of the union of the results. The hull operator ensures that the result remains a single interval, even when individual images from subintervals are disjoint.

$$f(\mathbf{X}) \subseteq \Diamond\left(\cup f(\mathbf{X}^{(i)})\right) \tag{57}$$

4) Refine iteratively: as N increases, dependency within each subinterval is reduced, and the enclosure contracts toward the true image of the function.

The convergence of piecewise interval evaluation is guaranteed for continuous functions; in the limit, the hull converges to the exact range (Yadav 2025), although for finite N it generally provides an enclosure. This strategy can also be used in validating numeric and interval finite element formulations, where dependency problems otherwise lead to meaningless results.

2.4.6 Step-by-step procedure in IFEM

1. Start / collect all existing information including:
   - Dam geometry and foundation profile
   - External loading conditions (dead load, hydrostatic pressure, uplift pressure, thermal loads, seismic loads if applicable)
   - Material properties ($\mathbf{E}$, ν)
   - Shear strength parameters ($\boldsymbol{\phi_r}$, $\mathbf{JRC}$, $\mathbf{JCS}$)
   - Represent uncertain parameters in interval form
2. Assume an uncracked interface (i.e., crack length, Lc = 0).

3. Calculate all external loads in interval form. Note: Uplift pressure distribution along the interface depends on crack length.
4. Define geometry, discretize the domain using appropriate finite element types and mesh sizes, and assign interval material properties.
5. Apply external loads.

Iterative crack update and uplift/Boundary Conditions (BCs) update

6. Apply BCs: restrain translation in both global X and Y directions at the boundary (concrete–foundation rock interface).
7. Solve using IFEM.
8. Check tensile condition: Is the interface under tension?
   If YES:
   a) Calculate the new crack length Lc (length of tensile zone or segment where shear strength < shear stress at the interface).
   b) Update and apply uplift pressure along the interface based on the current crack length Lc.
   c) Update BCs of the cracked interface:
      - Release translation in global X direction in all cases.
      - If tension: allow separation (release in global Y direction).
      - If compression: enforce no penetration (keep restraint in global Y direction).
   d) Go back to Step 7.
   If NO (i.e., no tension): continue to Step 9.
9. Calculate shear strength using compressive stress at the interface and the Barton–Choubey Shear Strength model.
10. Check shear crack criterion: Is computed shear strength < shear stress at the interface?
    If YES: Go back to Step 8a (update Lc, then uplift/BCs, then re-solve).
    If NO (i.e., crack length is converged): proceed to next step.
11. Check for the rigid body motion: Is entire interface in cracked?
    If Lc $\geq B_0$, the entire interface is cracked. Hence, the dam transforms into a rigid body motion, and the sliding factor of safety is taken as zero. The further computation ends here.
    If Lc $< B_0$, the entire interface is not cracked. Hence, the dam does not transform into a rigid body motion. Proceed to step 12 to compute **FSS**.

Post-convergence (sliding demand vs resistance and FSS calculation)

12. Obtain sliding force from interface reactions (or equivalently from applied external loads).
13. Calculate shear strength of the uncracked interface from compressive stress using the Barton–Choubey model.
14. Calculate resisting force by integrating shear strength over the uncracked portion of the interface.
15. Compute interval factor of safety against sliding (**FSS**) by comparing sliding and resisting forces.
16. End.

2. Case Study

The numerical illustration considers a concrete gravity dam constructed in 1962 within the Carolina Slate Belt, a northeast-trending geologic province composed of low-grade metamorphic, volcanic, and sedimentary rocks extending from southwestern Virginia to central Georgia. The dam geometry is shown in Figure 4, and the principal dimensions are summarized in Table 2. Sliding is evaluated along the concrete–foundation rock interface. The foundation consists primarily of basaltic tuffs from the Upper Volcanic Sequence and mafic tuffaceous argillite from the Volcanic Sedimentary Sequence.

A comprehensive site investigation conducted in 1993 provided the material parameters required for stability assessment. The program included exploratory drilling and core logging, laboratory testing of concrete samples to determine density and compressive strength, compressive strength testing of foundation rock, and direct shear testing to characterize joint shear strength. The resulting material properties adopted in the deterministic, Monte Carlo, and IFEM analyses are summarized in Table 1.

Table 1: Material Properties utilized in LEM, MCS and IFEM Analyses

Parameters	LEM	Mean value (X_{mean}) for PDF for MCS	IFEM
(γ_c), N/m^3	24,082.363	24,082.363	[23,480.304, 24,684.423]
(γ_w), N/m^3	9,745.953	9,745.953	[9,732.386 , 9,759.519]
$\tau_s = c + \sigma_n \tan \phi_p$ (MPa)	$\tau_s = 0.0235 + \sigma_n \tan 52.66°$	N/A	N/A
JRC	N/A	11.5	[10.925, 12.075]
JCS (MPa)	N/A	57.5	[56.062, 58.938]
ϕ_r	39.62°	39.62°,	[38.63°, 40.61°]
E_{avg} (MPa)	N/A	N/A	28,222.316
Poisson's ratio (ν)	N/A	N/A	0.2

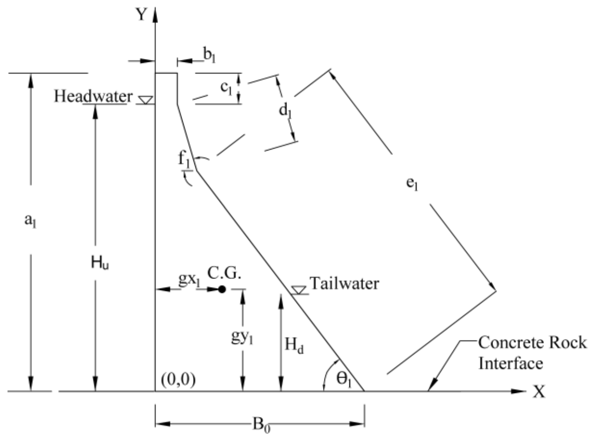

Figure 4: Geometry of the concrete gravity dam section under consideration

Segment	Length
a_1	26.18 m (85.9 ft)
b_1	1.83 m (6 ft)
c_1	2.56 m (8.4 ft)
d_1	5.71 m (18.73 ft)
e_1	22.71 m (74.50 ft)
B_0	17.22 m (56.5 ft)
Slope	**Angle**
f_1	74°
θ_1	53°

Table 2: Dimensions of dam geometry under consideration

Spatial variability of the modulus of elasticity (E) is particularly relevant in hydraulic structures due to long-term moisture exposure, especially near the upstream face. Previous studies (Sokolov and Rasskazchikov, 1986) documented moisture penetration depths of 4–6 m from the upstream face, with moisture content varying from approximately 1.5% at the heel to 0.1% near the downstream toe. These variations significantly influence stiffness and stress distribution along the concrete–rock interface.

Based on these observations, a linear spatial variation of moisture content $M_c(X, Y)$ is adopted, ranging from 0.1% at the water surface and toe to 1.5% at the heel. Following Liu et al. (2014), the Young's modulus is expressed as:

$$E(X, Y) = 1982.3M_c(X, Y) + E_{avg} \tag{58}$$

where E_{avg} is the average elastic modulus in MPa.

To reduce overestimation, the following stepwise approach is used. First, the deterministic Young's modulus is computed at each nodal coordinate using Equation (58). Then, the nodal values are interpolated to integration (Gauss) points using standard shape functions:

$$E_{Int\_pts} = N(\xi, \eta) \times E_{Nodal\_Coordinates} \tag{59}$$

where $N(\xi, \eta)$ denotes the matrix of shape functions in local co-ordinates, and $E_{Nodal\_Coordinates}$ represents the vector of elastic moduli at the element nodes.

To incorporate uncertainty, a variation of $\pm 2.5\%$ is applied on E_{Int_pts}, giving a total variation of 5%. Accordingly, the modulus of elasticity in interval form at the integration points is expressed as

$$\mathbf{E}_{Int\_pts} = E_{Int\_pts}[0.975, 1.025] \tag{60}$$

This formulation enables consistent comparison of deterministic, probabilistic, and interval-based stability assessments while explicitly accounting for spatial stiffness variation.

3. Results and Discussion

The dam section was discretized using 108 eight-node quadrilateral isoparametric elements (Figure 5). Spatial variability of Young's modulus, derived from moisture-dependent stiffness, is shown in Figure 6 using mid-interval values. External loads included self-weight, hydrostatic pressures, and uplift. The initial hydrostatic and uplift distributions (zero crack length assumption) are presented in Figure 7.

Crack initiation was evaluated based on tensile stress and shear stress exceeding interface shear strength. As cracking developed, boundary conditions and uplift distribution were iteratively updated within the IFEM framework. The converged uplift profile and crack configuration are shown in Figure 8. Convergence was achieved in three iterations.

The final crack length was 3.1309 m (18.18% of the 17.22 m base). The computed interval sliding factor of safety was $\mathbf{FSS} = [3.104, 4.938]$, indicating stability for all admissible parameter bounds. Stress distributions on the deformed configuration are shown in Figures 9 through 11. Cracked segments under tension provide no shear resistance, while uncracked compressive regions maintain shear strength exceeding the applied shear stress.

In contrast, the crack-based LEM predicted a crack length of 16.564 m (96.19% of the base) with FSS $= 0.086$, indicating instability. This discrepancy stems from the linear Mohr–Coulomb assumption and simplified crack initiation and propagation criterion in LEM. Even when peak Mohr–Coulomb strength parameters from laboratory tests were adopted, LEM predicted nearly full-base cracking and FSS < 1. The predicated instability becomes more pronounced when residual friction angle and zero cohesion are used, as commonly assumed in practice.

The Monte Carlo simulation with 2×10^6 realizations yields factor of safety at the 5th, 50th, and 95th percentiles of $\mathrm{P}_5 = 1.49, \mathrm{P}_{50} = 1.83$ and $\mathrm{P}_{95} = 2.16$, respectively, while the probability of failure ($\mathrm{P}(\mathrm{FSS} < 1)$) is zero. The Monte Carlo simulation predicted a mean crack length of 3.11 m, corresponding to the 95th percentile, which differs from the IFEM result (3.13 m) by about 0.64%. This close agreement in crack length indicates that the IFEM has efficiently captured the uplift–crack coupling, resulting in a more realistic prediction of crack propagation. By comparison, the interval finite element method produces a factor of safety enclosure of $[3.104, 4.938]$. The factor of safety is lower in the Monte Carlo simulation because the formulation compares lumped angles. In contrast, IFEM integrates the stress-dependent BC shear strength distribution along the uncracked interface, leading to a resistance evaluation consistent with local stress states rather than a single resultant-based comparison. Since the interval **FSS** is entirely greater than unity, no admissible parameter realization within defined bounds results in sliding failure. IFEM therefore provides a guaranteed safety bound, while the MCS offers probabilistic insight into the most likely outcomes under the same interval bounds. Together, the two approaches confirm that the structure remains stable under the full range of interval-defined uncertainty, whereas the limit equilibrium method (LEM) predicts almost the entire base to be cracked and the dam to be unstable. This contrast highlights the importance of the IFEM approach proposed in this paper, as it provides a more realistic and reliable assessment of dam stability.

4. Conclusions

This study presented a comparative evaluation of deterministic crack-based Limit Equilibrium Method (LEM), Monte Carlo Simulation (MCS), and an Interval Finite Element Method (IFEM) for sliding stability analysis of concrete gravity dams, incorporating iterative uplift–crack coupling through boundary-condition updates. The conventional LEM, based on linear Mohr–Coulomb strength and resultant-force-based crack estimation, predicted extensive cracking and a factor of safety below unity for the considered parameter set. The Monte Carlo framework provided realistic percentile-based safety factors but required extensive sampling and probabilistic input assumptions.

The proposed IFEM integrates the nonlinear Barton–Choubey shear strength model, interval representation of uncertain parameters, piecewise treatment to control overestimation, element-by-element assembly, and iterative crack–uplift coupling. The method captured tensile and shear cracking mechanisms while consistently updating uplift redistribution. For the case study, IFEM predicted limited cracking and an interval factor of safety entirely greater than unity, consistent with Monte Carlo results and observed dam performance.

Unlike LEM, IFEM does not rely on simplified resultant-force assumptions, and unlike MCS, it does not require probability density functions. Instead, it provides mathematically guaranteed safety bounds using only upper and lower parameter limits, offering a computationally efficient and reliable framework for sliding stability assessment under bounded uncertainty.

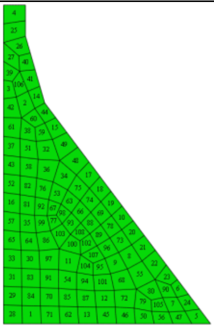

Figure 5: Finite element mesh of dam geometry (8-node quadrilateral isoparametric elements)

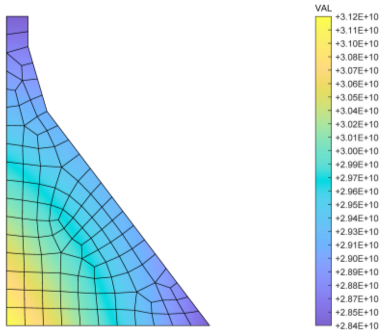

Figure 6: Spatial variation of modulus of elasticity (E) within the dam body due to moisture content, plotted using mid-interval values

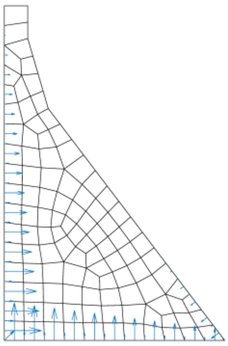

Figure 7: Hydrostatic and uplift pressure distributions for the first iteration with zero crack length

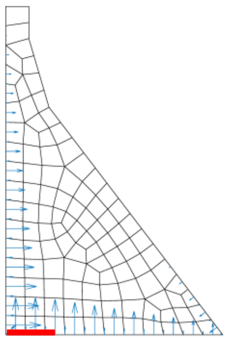

Figure 8 Hydrostatic and updated uplift pressure distributions under the converged crack state. Note the uniform uplift pressure along the cracked interface shown in red

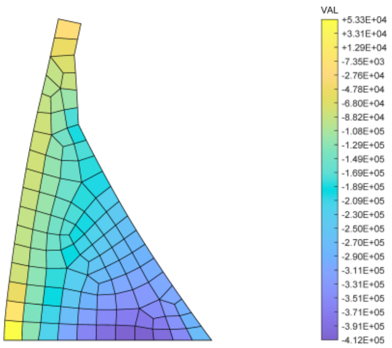

Figure 9: Distribution of $\boldsymbol{\sigma_{YY}}$ *(normal stress in Y-direction) on the deformed dam shape, plotted using mid-interval values*

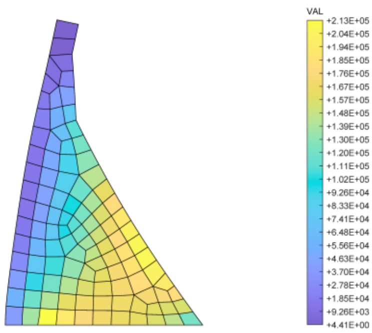

Figure 10: Distribution of $\boldsymbol{\tau}$ *(shear stress) on the deformed dam shape, plotted using mid-interval values*

References

Alefeld, G. and J. Herzberger (1983). Introduction to Interval Computations. New York, Academic Press.

Ali, M. H., M. R. Alam, M. N. Haque and M. J. Alam (2012). "Comparison of Design and Analysis of Concrete Gravity Dam." Natural Resources 3(1): 30–36.

Barton, N. (1973). "Review of a new shear-strength criterion for rock joints." Engineering Geology 7(4): 287–332.

Barton, N. (1974). A review of the shear strength of filled discontinuities in rock. Norwegian Geotechnical Institute. Bergmekanikk, Oslo.
Barton, N. (1976). "The shear strength of rock and rock joints." International Journal of Rock Mechanics and Mining Sciences & Geomechanics Abstracts 13(9): 255–279.
Barton, N. (2013). "Shear strength criteria for rock, rock joints, rockfill and rock masses: Problems and some solutions." Journal of Rock Mechanics and Geotechnical Engineering 5(4): 249–261.
Barton, N. (2016). "Non-linear shear strength for rock, rock joints, rockfill and interfaces." Innovative Infrastructure Solutions 1(1): 30.
Barton, N. and S. Bandis (1982). "Effect of block size on the shear behavior of jointed rocks." Proceedings - Symposium on Rock Mechanics: 739–760.
Barton, N. and V. Choubey (1977). "The shear strength of rock joints in theory and practice." Rock Mechanics Felsmechanik Mecanique des Roches 10(1-2): 1–54.
Barton, N., C. Wang and R. Yong (2023). "Advances in joint roughness coefficient (JRC) and its engineering applications." Journal of Rock Mechanics and Geotechnical Engineering 15(12): 3352–3379.
Barton, N. R. and S. C. Bandis (1990). Review of predictive capabilities of JRC-JCS model in engineering practice. Rock Joints. N. Barton and O. Stephansson. Rotterdam, Balkema.
De Sazilly, J. A. T. (1853). "Note sur un type de profil d'égale résistance, proposé pour les murs de réservoirs d'eau (Note on a profile of equal resistance proposed for water reservoir walls)." Journal: Annales des ponts et chaussées **6**(2e semestre): 191–222.
Federal Energy Regulatory Commission (2015). Chapter 1 - General Requirements of Engineering Guidelines for the Evaluation of Hydropower Projects. Washington, DC, Federal Energy Regulatory Commission (FERC).
Federal Energy Regulatory Commission (2016). Chapter 3 – Gravity Dams of Engineering Guidelines for the Evaluation of Hydropower Projects. Washington, DC, Federal Energy Regulatory Commission (FERC).
Fell, R., P. MacGregor, D. Stapledon, G. Bell and M. Foster (2015). Goetechnial Engineering of Dams. Boca Raton, FL, CRC Press.
Kulisch, U. W. and W. L. Miranker (1981). INTERVAL ARITHMETIC. Computer Arithmetic in Theory and Practice, Elsevier: 84–151.
Liu, B. D., W. J. Lv, L. Li and P. F. Li (2014). "Effect of moisture content on static compressive elasticity modulus of concrete." Construction and Building Materials 69: 133–142.
Mallela, V. R. R., R. L. Mullen and R. L. Muhanna (2011). "A new interval finite element formulation with the same accuracy in primary and derived variables." International Journal of Reliability and Safety 5(4): 347–360.
Moore, R. E. (1966). Interval Analysis. Englewood Cliffs, NJ, Prentice Hall.
Moore, R. E. (1979). Methods and Applications of Interval Analysis. Philadelphia, SIAM.
Muhanna, R., V. R. R. Mallela and R. Mullen (2013). "Advances in Interval Finite Element Modelling of Structures." 2: 15–22.
Muhanna, R. L. and R. L. Mullen (2001). "Uncertainty in Mechanics Problems—Interval–Based Approach." Journal of Engineering Mechanics 127(6): 557–566.
Muhanna, R. L., H. Zhang and R. L. Mullen (2007). "Combined Axial and Bending Stiffness in Interval Finite-Element Methods." Journal of Structural Engineering 133(12): 1700–1709.
Muhanna, R. L., H. Zhang and R. L. Mullen (2007). "Interval Finite Elements as a Basis for Generalized Models of Uncertainty in Engineering Mechanics." Reliable Computing 13(2): 173–194.
Nallanathel, M., B. Ramesh and P. K. A. Raju (2018). "Stability Analysis of Concrete Gravity Dam Using STAAD Pro." International Journal of Pure and Applied Mathematics 119(17): 297–310.
Neumaier, A. (1990). Interval Methods for Systems of Equations, Cambridge University Press.
Rao, M. V. R., R. L. Mullen and R. L. Muhanna (2011). "A new interval finite element formulation with the same accuracy in primary and derived variables." International Journal of Reliability and Safety 5(3/4): 336.
Rump, S. M. (1999). "Fast and Parallel Interval Arithmetic." BIT Numerical Mathematics 39(3): 534–554.
Rump, S. M. (1999). INTLAB - Interval Laboratory. Developments in Reliable Computing. Dordrecht, Netherlands, Kluwer Academic Publishers: 77–104.
Sokolov, I. B. and V. A. Rasskazchikov (1986). "Consideration of moisture effects on the upstream face of concrete dams." Hydrotechnical Construction 20(3): 193–198.
U.S. Army Corps of Engineers (2005). Stability Analysis of Concrete Structures. Washington, D.C.
United States Bureau of Reclamation (1987). Design of Small Dams. Denver, CO, United States Department of the Interior, Bureau of Reclamation.
Weijermars, R. (1997). Principles of Rock Mechanics, Alboran Science Publishing.
White, F. M. (2011). Fluid Mechanics. New York, NY, McGraw-Hill.
Xiao, N. (2015). Interval Finite Element Approach for Inverse Problem under Uncertainty. PhD Thesis, Georgia Institute of Technology.
Xiao, N., F. Fedele and R. Muhanna (2016). "Interval-based parameter identification for structural static problems." 23: 47–72.
Xiao, N., R. Muhanna, F. Fedele and R. Mullen (2015). "Interval Finite Element Analysis of Structural Dynamic Problems." SAE International Journal of Materials and Manufacturing 8.
Yadav, B. (2025). Interval Finite Element Approach for Stability Analysis of Concrete Gravity Dams under Uncertainties. PhD Thesis, Georgia Institute of Technology.